Computational methods in welding and additive manufacturing/Simulation numérique des procédés de soudage et de fabrication additive

A two-dimensional simulation of grain structure growth within the substrate and the fusion zone during direct metal deposition

Jingwei Zhang, Wei Li, Lei Yan, Frank Liou

Department of Mechanical and Aerospace Engineering, Missouri University of Science and Technology, Rolla, MO, 65401, USA

A R T I C L E   I N F O

A B S T R A C T

In this paper, a predictive multi-scale model based on a cellular automaton (CA)-finite element (FE) method has been developed to simulate thermal history and microstructure evolution during metal solidification for the Direct Metal Deposition (DMD) process. The macroscopic FE calculation that is validated by thermocouple experiment is developed to simulate the transient temperature field and cooling rate of single layer and multiple layers. In order to integrate the different scales, a CA–FE coupled model is developed to combine with thermal history and simulate grain growth. In the mesoscopic CA model, heterogeneous nucleation sites, grain growth orientation and rate, epitaxial growth, re-melting of pre-existing grains, metal addition, grain competitive growth, and columnar to equiaxed phenomena are simulated. The CA model is able to show the entrapment of neighboring cells and the relationship between undercooling and the grain growth rate. The model predicts the grain size, and the morphological evolution during the solidification phase of the deposition process. The developed "decentered polygon" growth algorithm is appropriate for the non-uniform temperature field. Finally, the single and multiple-layer DMD experiment is conducted to validate the characteristics of grain features in the simulation.

© 2018 Académie des sciences. Published by Elsevier Masson SAS. All rights reserved.

1. Introduction

Compared with the conventional subtractive manufacturing technologies, additive manufacturing (AM) has unique advantages including low heat input, small heat-affected zone, solid-free-form fabrication, near-net-shape, and so on. Direct Metal Deposition (DMD), a rapid developing AM technique, is able to manufacture a fully dense metal part without intermediate steps, which is especially appropriate for manufacturing heterogeneous components. During the deposition process, solidification thermodynamics determined by a series of process parameters affect microstructure evolution, which directly affects the mechanical properties of the materials. The temperature field history and the cooling rate are the key factor for controlling the solidification microstructure after the DMD process [1]. Several approaches, either stochastic or deterministic, have been taken to model solidification microstructure evolution. Anderson et al. [2,3] developed a Monte Carlo (MC) stochastic method to simulate the grain growth, topology, grain size distribution, curvature and grain velocities, as well as their interrelationships. Saito and Enomoto [4] incorporated the anisotropy of the grain boundary energy, the pinning effect

of precipitates on growth kinetics into the MC simulation. Another idea of modeling is the deterministic approach. Chen [5] investigated a phase-field (PF) method to model and predict mesoscale morphological and microstructure evolution in materials. Krill et al. [6–8] developed PF to simulate 2D grain growth, 3D gain growth, equiaxed solidification. However, a phase field model [9,10] usually carries a very high computational cost because of a requirement for a particularly fine computational grid.

In order to reduce the computational cost, RAPPAZ and GANDIN [11] put forward a two-dimensional cellular automaton approach to model grain structure formation in the solidification process. The model includes the mechanisms of heterogeneous nucleation and of grain growth. Nucleation occurring at the interface as well as in the liquid metal is treated by using two distributions of nucleation sites. The location and the crystallographic orientation of the grains are chosen randomly among a large number of cells and a certain number of orientation classes, respectively. However, the model was then applied to small Al–7wt%Si specimens of uniform temperature. In order to develop the non-uniform temperature prediction, Gandin et al. [12] proposed a 2-dimensional Cellular Automaton (CA) technique for the simulation of dendritic grain formation during solidification. The non-uniform temperature situation was fully coupled with an enthalpy-based Finite Element (FE) heat flow calculation. This progress made it possible to combine the temperature field history with the microstructure evolution. The coupled CA–FE model is applied to an Al–7wt%Si alloy. A three-dimensional CA–FE model predicting the dendritic grain structures formed during solidification [13] was analyzed. The potentiality of the CA–FE model is demonstrated through the prediction of typical grain structures formed during the investment casting and continuous casting processes. Based on the features of several developing approaches, Choudhury et al. [14] compared a CA model with a PF model for simulations of the dendritic solidification of an Al–4wt%Cu alloy, two- and three-dimensionally for different undercooling situations. In 2D, the tip properties simulated using the PF model show excellent agreement. At high undercooling, the CA model becomes advantageous, as its reproduction of the theoretical behavior improves. As the CA model is capable of simulating at coarse scales in a comparably short time, its output can be used as an input for a PF simulation for resolving finer details of microstructure formation. This can be utilized to build a hybrid model to integrate CA high efficiency and PF accuracy. Dore [15] investigated the quantitative prediction of micro-segregation during the solidification of the ternary alloy system, and applied it to the solidification of Al–Mg–Si. Jarvis et al. [16] firstly compared 1D, 2D, and 3D cellular automaton finite difference (CA–FD) simulations of the non-equilibrium solidification in an Al–3.95Cu–0.8Mg ternary alloy. It has been demonstrated that there is good agreement between all CA–FD models in terms of primary α-Al phase. However, the final dendrite arm spacings are slightly overestimated in 2D and 3D.

High cooling rate and non-equilibrium is a typical characteristic of the DMD technique comparing the conventional casting process and simulation. Grujicic et al. [17] proposed a modified CA-based method to investigate the evolution of the solidification grain microstructure during the LENS rapid fabrication process. This research established the relationship between process parameters (e.g., laser power, laser velocity) and solidification microstructure in binary metallic alloys. The finite difference analysis was also coupled with the modified CA to calculate the temperature field as the input of microstructure prediction. Kelly et al. [18,19] developed the thermal history in DMD of Ti6Al4V and microstructural characterization. Tan et al. [20] developed a multi-scale model to study the growth of grains and sub-grain dendrites of austenitic stainless steel during laser keyhole welding process. Chen et al. [21,22] developed a 3D coupled CA–FE model for the solidification grain structure during Gas Tungsten Arc Welding (GTAW). During the simulation, the parallel computations and dynamic strategies for the allocation of CA grids are employed to optimize the computer memories. It provides the possibility of handling domains with millions of grains inside. Zinoviev et al. [23] investigated a two-dimensional numerical model to simulate the grain structure evolution during a selective laser melting process. The equiaxed and columnar grains, which is validated by the experimental result, can be achieved within the melt pool. However, there are few investigations on microstructure evolution prediction based on the whole deposit part during the DMD process. This part-level simulation on microstructure is critical because it provides the foundation for predicting and controlling the mechanical properties.

In this study, a predictive multi-scale model based on a Cellular Automaton (CA)-Finite Element (FE) method has been developed to simulate the thermal history and microstructure evolution during metal solidification in the frame of a laser-based additive manufacturing process. ABAQUS was used to calculate the temperature field of the whole part, which offers the macroscopic FE nodes' temperature. In order to integrate the different scales, a coupled model is developed to combine with thermal history and simulate nucleation site, grain growth orientation and rate, epitaxial growth of new grains, remelting of preexisting grains, metal addition, and grain competitive growth. Interpolation was utilized to obtain the finer nodes' temperature based on the FE nodes result. The temperature field was validated by type-K thermocouples. The CA model, which was able to show the entrapment of the neighboring cells and the relationship between undercooling and grain growth rate, was built to simulate microstructure information, such as grain size and columnar grain orientation. The developed "decentered polygon" algorithm is more appropriate for grain structure development in the highly non-uniform temperature field. This simulation will lead to new knowledge that simulates the grain structure development of single-layer and multiple-layer deposition during the DMD process. The microstructure simulation results were validated by the experiment. The model parameters for the simulations were based on a Ti–6Al–4V material (Fig. 1).
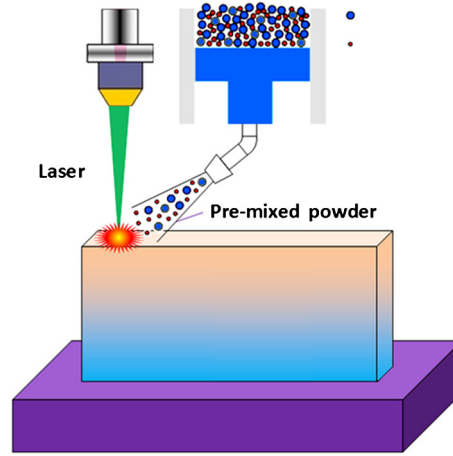
Fig. 1. Laser powder deposition schematic.

2. Mathematical model

2.1. Ti6Al4V transient temperature field during the deposition process

In the Direct Metal Deposition (DMD) process, the temperature history of the whole domain directly influences the deposition microstructure, which is critical to mechanical properties [24]. In order to obtain the microstructure information during the solidification process, the temperature field must be known at each time step. The transient temperature field throughout the domain was obtained by solving the 3D heat conduction equation – Eq. (1) – in the substrate, along with the appropriate initial and boundary conditions [25]:

$$\rho(T) \cdot c_p(T) \cdot \frac{\partial T}{\partial T} = \frac{\partial}{\partial x}\left(k(T)\frac{\partial T}{\partial x}\right) + \frac{\partial}{\partial y}\left(k(T)\frac{\partial T}{\partial y}\right) + \frac{\partial}{\partial z}\left(k(T)\frac{\partial T}{\partial z}\right) + \dot{Q} \tag{1}$$

where T is the temperature, $\rho(T)$ is the density, $c_p(T)$ is the specific heat, $k(T)$ is the heat conductivity, and Q is the internal heat generation following certain energy distribution per unit volume.

2.1.1. Initial conditions and boundary conditions

The initial conditions applied to solve Eq. (2) were:

$$T(x, y, z, 0) = T_0 \quad \text{and} \quad T(x, y, z, \infty) = T_0 \tag{2}$$

where T_0 is the ambient temperature. In this study, T_0 was set as room temperature, 298 K. The boundary conditions, including thermal convection and radiation, are described by Newton's law of cooling and the Stefan–Boltzmann law, respectively. The laser heating source term, $\dot{Q}$ in Eq. (1), was also considered in the boundary conditions as a surface heat source. The boundary conditions then could be expressed as [25]:

$$K(\Delta T \cdot n)|_\Gamma = \begin{cases} [-h(T - T_0) - \varepsilon(T)\sigma(T^4 - T_0^4)]|_\Gamma & \Gamma \notin \Lambda \\ [Q - h(T - T_0) - \varepsilon(T)\sigma(T^4 - T_0^4)]|_\Gamma & \Gamma \in \Lambda \end{cases} \tag{3}$$

where k, T, T_0, and Q bear their previous definitions, n is the surface normal vector, h is the heat convection coefficient, $\epsilon(T)$ is the emissivity, σ is the Stefan–Boltzmann constant, which is 5.6704×10^{-8} W/m^2 K^4, Γ represents the surfaces of the work piece, and Λ represents the surface area irradiated by the laser beam.

2.1.2. Assumptions

To simulate the thermal history during Direct Metal Deposition more efficiently and to reduce the computational cost, some assumptions were considered. In the experiment, a Gaussian-distributed laser beam was utilized to melt the substrate vertically with a non-uniform power density. [26] Thus, the transverse intensity variation is described as Eq. (4):

$$I(r, y) = \alpha \frac{P}{\pi w(y)^2/2} \exp\left(-2\frac{r^2}{w(y)^2}\right) \tag{4}$$

where α is the laser absorption coefficient, P is the power of the continuous laser, and $w(y)$ is the distance from the beam axis where the optical intensity drops to $1/e^2$ ($\approx 13.5\%$) of the value on the beam axis. α was set as 0.4 based on

numerical experiments in the LAMP lab, and $w(y)$ is 1 mm in this simulation. The motion of the laser beam was simulated by adjusting the position of the beam center R with programming a user subroutine "DFLUX" in ABAQUS. The formula of R is as follows:

$$R = \left[\left(x - \int_{t_0}^{t} u\,\mathrm{d}t \right) + \left(y - \int_{t_0}^{t} v\,\mathrm{d}t \right) + \left(z - \int_{t_0}^{t} w\,\mathrm{d}t \right) \right]^{1/2} \tag{5}$$

where x, y, and z are the spatial coordinates of the Gaussian laser beam center, and u, v, and w are the laser's moving velocities.

The influence of the latent heat of fusion during the melting/solidification process was described by the modified specific heat. The equivalent specific heat c_p^* is calculated by

$$c_p^*(T) = c_p(T) + \frac{L}{T_m - T_0} \tag{6}$$

where $c_p^*(T)$ is the modified specific heat, $c_p(T)$ is the original temperature-dependent specific heat, L is the latent heat of fusion, T_m is the melting temperature, and T_0 is the ambient temperature.

The Marangoni effect caused by the thermocapillary phenomena can directly influence the temperature field in the whole domain, so it is taken into account to obtain a more accurate thermal history during DMD. [27] The artificial thermal conductivity was put forward to addressing the Marangoni effect in the finite element method [28]

$$k_m(T) = \begin{cases} k(T), & T \le T_{\text{liq}} \\ 2.5k(T), & T > T_{\text{liq}} \end{cases} \tag{7}$$

where k_m is the modified thermal conductivity, and T_{liq} is the liquidus temperature.

In the FEA model, the powder addition was simulated by activating elements in many small steps [29]. The width of the deposit area is assumed to be the same as the Gaussian laser beam. The thickness of each layer is calculated by transverse speed, powder feed rate, and powder absorption efficiency. The deposit geometry, boundary condition, and heat flux was updated after each step.

2.2. Ti6Al4V morphology prediction after solidification

Heterogeneous nucleation occurs nearly instantaneously at a characteristic undercooling. The locations and crystallographic orientation of the new nuclei are randomly chosen at the surface or in the liquid. As explained by Oldfield [30], the continuous nucleation distribution, $\mathrm{d}n/\mathrm{d}\Delta T'$, which characterizes the relationship between undercooling and the grain density, is described by a Gaussian distribution both at the mold wall and in the bulk liquid. The parameters of these two distributions, including maximum nucleation density $n_{\max}$, the mean undercooling ΔT_N, and the standard deviation of the grain density distribution ΔT_σ, can be obtained from experiments and grain size measurements. The governing equation of nucleation is shown in Eq. (8), which describes the grain density, $n(\Delta T)$:

$$n(\Delta T) = \int_{0}^{\Delta T} \frac{\mathrm{d}n}{\mathrm{d}\Delta T'}\mathrm{d}\Delta T' = \int_{0}^{\Delta T} \frac{n_{\max}}{\Delta T_\sigma \sqrt{2\pi}} \exp\left[-\frac{1}{2}\left(\frac{\Delta T' - \Delta T_N}{\Delta T_\sigma} \right) \right]\mathrm{d}\Delta T' \tag{8}$$

where $n_{\max}$ is the maximum nucleation density of nucleation grains, which is obtained by the integral of the nucleation distribution (from zero undercooling to infinite undercooling). ΔT_N and ΔT_σ are the mean undercooling and standard deviation of the grain density distribution, respectively. Here, all temperatures are in Kelvin.

Undercooling is the most important factor in the columnar and dendrite growth rate and grain size. The total undercooling of the dendritic tip consists of three parts: solute undercooling, thermal undercooling, and curvature undercooling. For most metallic alloys, the kinetic undercooling for atom attachment is small, so it is neglected [31]. The total undercooling can be calculated as follows:

$$\Delta T = mC_0\left[1 - A(P_c) \right] + \theta_T I(P_T) + \frac{2\Gamma}{R} \tag{9}$$

where m is the liquidus slope, Γ is the Gibbs–Thomson coefficient, C_0 is the solute concentration in the liquid far from the solid–liquid interface, P_T and P_c are the thermal and solutal Péclet numbers, respectively, k is the solute partition coefficient at the solid–liquid interface; $A(P_c)$ equals $[1 - (1-k)I(P_c)]^{-1}$, θ_T is the unit thermal undercooling $(= \Delta h_f/c)$, and R is the radius of the dendritic tip.

For the laser deposition process, the rapid solidification condition corresponds to a high Péclet number at which the dendritic tip radius is given by Eq. (10), which is a governing equation for grain growth,
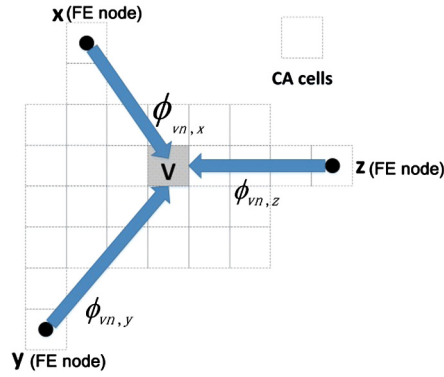
Fig. 2. x, y, and z represents the FE temperature nodes (coarse grids), and v represents the CA cells (fine grids). The three linear interpolation coefficients from FE nodes x, y, z to CA cells v are $\phi_{vn,x}$, $\phi_{vn,y}$, and $\phi_{vn,z}$.

$$R = \left[\frac{\Gamma}{\sigma^*(mG_c^* - G^*)} \right]^{1/2} \tag{10}$$

where σ^*, the marginal stability constant, approximately equals $1/4\pi^2$ [32], and G^* and G_c^* are the effective temperature gradient and concentration gradient, respectively.

2.3. Coupling macroscopic FE and mesoscopic CA models

The temperature field result can be used to calculate the enthalpy increment, which is necessary to calculate enthalpy at each time step. A linearized implicit FE enthalpy formulation of the heat flow equation can be given by equation (11) in Ref. [12]

$$\left[\frac{1}{\Delta t} \cdot [M] + [K]^t \left[\frac{\partial T}{\partial H} \right]^t \right] \cdot \{\delta H\} = -\{K\}^t \cdot \{T\}^t + \{b\}^t \tag{11}$$

where $\{M\}$ is the mass matrix; $\{K\}$ is the conductivity matrix; $\{b\}$ is the boundary condition vector; and $\{T\}$ and $\{H\}$ are the temperature and enthalpy vectors at each node of the FE mesh, respectively. The Newton Method and Euler implicit iteration are included in (11). This set of equations can be solved using the Gauss elimination method for $\{\delta H\}$.

$$\delta H = \rho \cdot c_p \cdot \left[T^{t+\delta t} - T^t \right] - \Delta H_f \cdot \delta f_s \tag{12}$$

Thus, the next time-step enthalpy can be obtained by the relationship: $H_i^{t+1} = H_i^t + \delta H$. The new temperature field can be obtained from the coupling model using (12). ΔH_f is the latent heat of fusion per unit volume. f_s represents the fraction of solid. δf_s can be calculated as in [12].

In the FE macroscopic model, the temperature field was calculated on a relatively coarse mesh, but the solidification microstructure had to be developed on a finer regular CA mesh with a cell size of the order of the secondary dendrite arm spacing (SDAS). Fig. 2 indicates the interpolated relationship between coarse FE nodes and fine CA cells. The known temperature T_n^t and the volumetric enthalpy variation δH_n were interpolated into the CA network by the linear interpolation in Eqs. (13) and (14). ϕ_{vn} is the interpolation coefficient. Every CA cell temperature in the calculation domain can be obtained with this interpolation.

$$T_v^t = \sum_n \phi_{vn} \cdot T_n^t \tag{13}$$

$$H_v^t = \sum_n \phi_{vn} \cdot H_n^t \tag{14}$$

The finer temperature, T_v^t, and enthalpy variations δH_v^t in regular CA cells were used in Eq. (14) to yield the temperature in the next micro time step. After a few micro time steps, the temperature field in the CA network could be substituted into the coarser nodes of the macroscopic model. The interpolated temperature field is employed as the model input. Heterogeneous nucleation, grain growth orientation, and grain growth are solved in the CA–FE model in terms of nucleation location distribution, random crystallographic orientation, and CA cells capture. Fig. 3 indicates the flow chart of the coupling FE–CA model. The details of CA growth algorithm are shown in Fig. 4.

Fig. 5 illustrates the conventional and modified cell capture algorithm. For the conventional method, the vertex of the square envelope moves along the diagonal, and the growth of the square envelope is determined by the center cell temperature, not the local temperature, at each time step, which results in the same growth rate for the four vertices. The
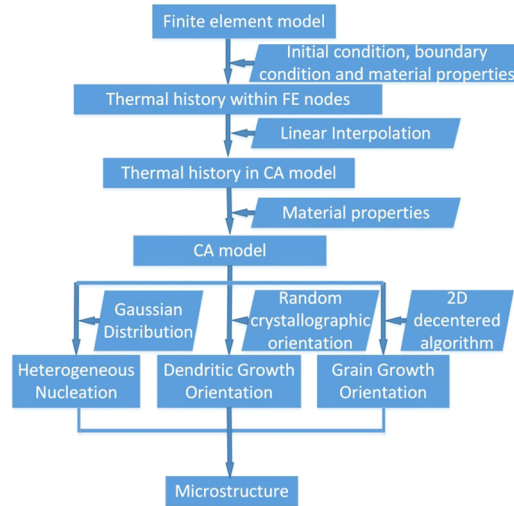
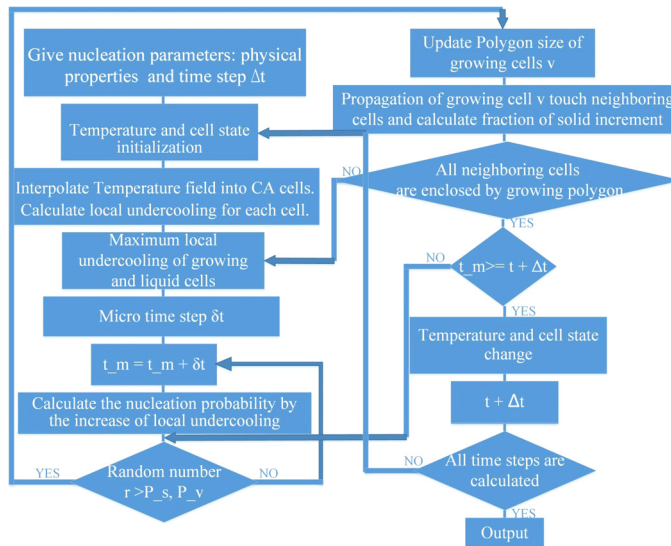**Fig. 3.** Flow chart of the coupling CA–FE model.

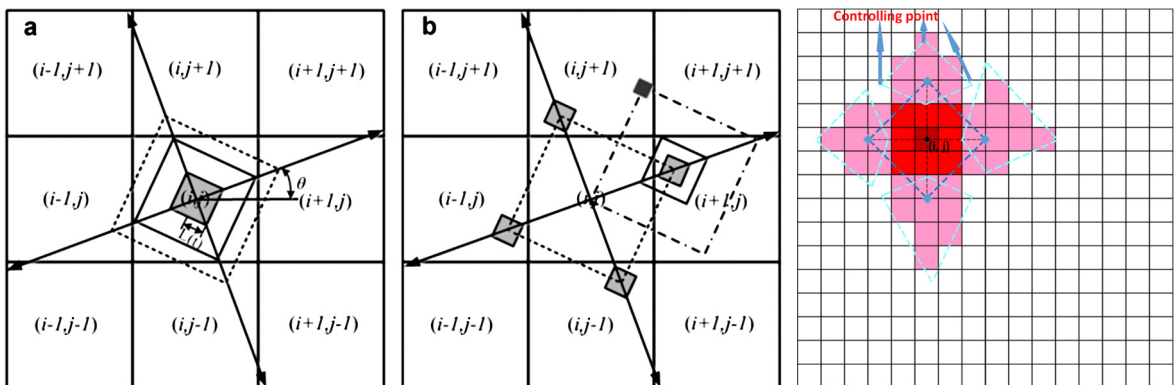**Fig. 4.** Flow chart of CA algorithm.

Fig. 5. Illustration of the conventional and modified cell capture algorithm: (a) capturing rule of cell (i, j) within a decentered square, (b) capturing rule of 8 neighboring cells before (i, j) growth termination [33], (c) the modified cell capture and growth algorithm of the "decentered polygon" with neighboring cell effect for cubic crystal alloys.
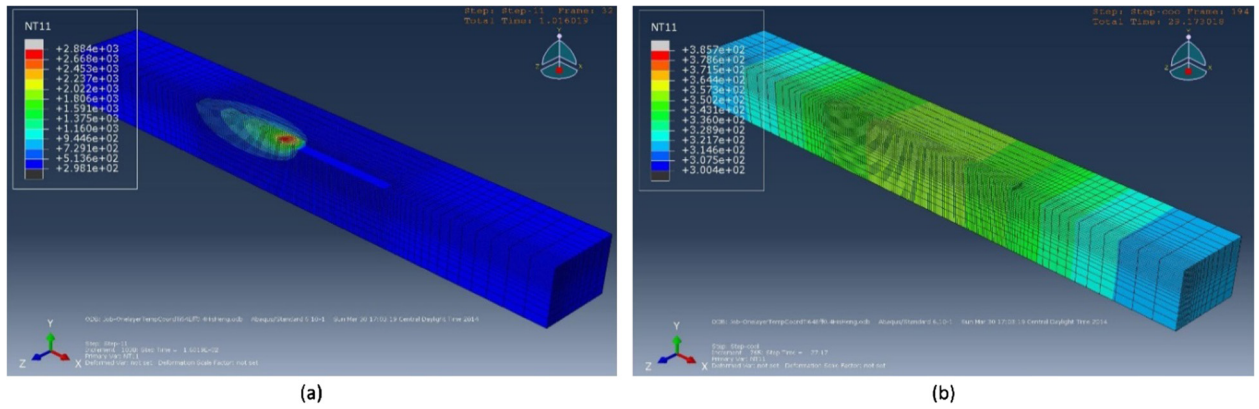
Fig. 6. Cross sectional simulated temperature distribution during the single-layer laser-deposition process. The deposition time is 2 s, while the cooling time is 28 s. (a) Temperature field at time = 1.0 s (b) Temperature field at time = 29.0 s.
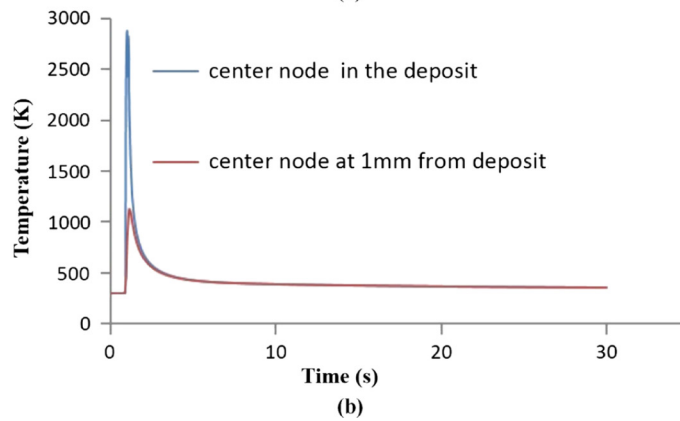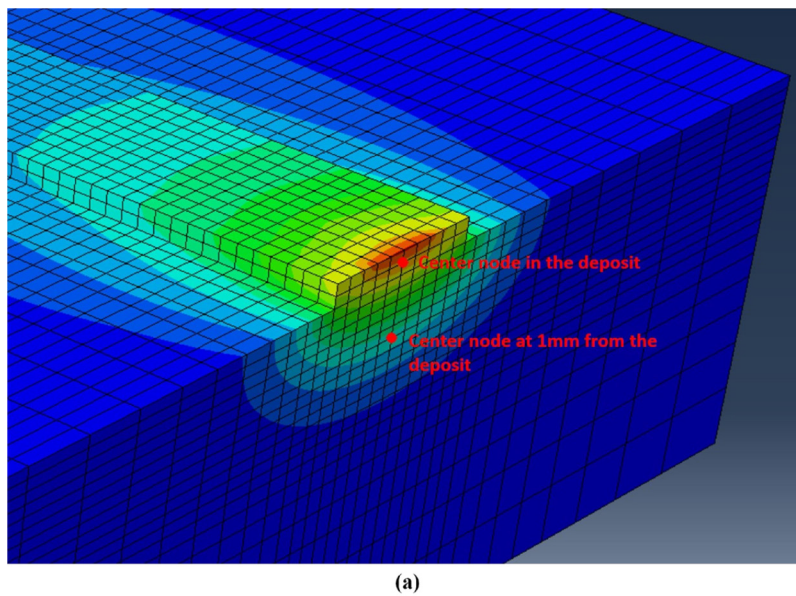

Fig. 7. Temperature history at the center node in the deposit and the substrate during the deposition and cooling processes.

grain orientation will be along the axis of computational domain after a few time steps, thus losing its original orientation information. The modified "decentered polygon" algorithm is implemented to control the grain growth within the melt pool and at the sold/liquid interface. Compared to the traditional "decentered square" algorithm of cell capturing, the modified
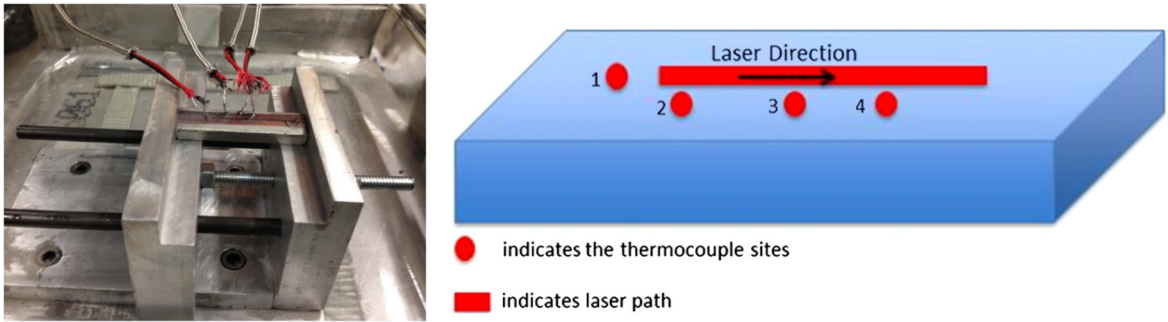
Fig. 8. Schematic diagram showing the location of the thermocouples location and the direction of the laser scan.
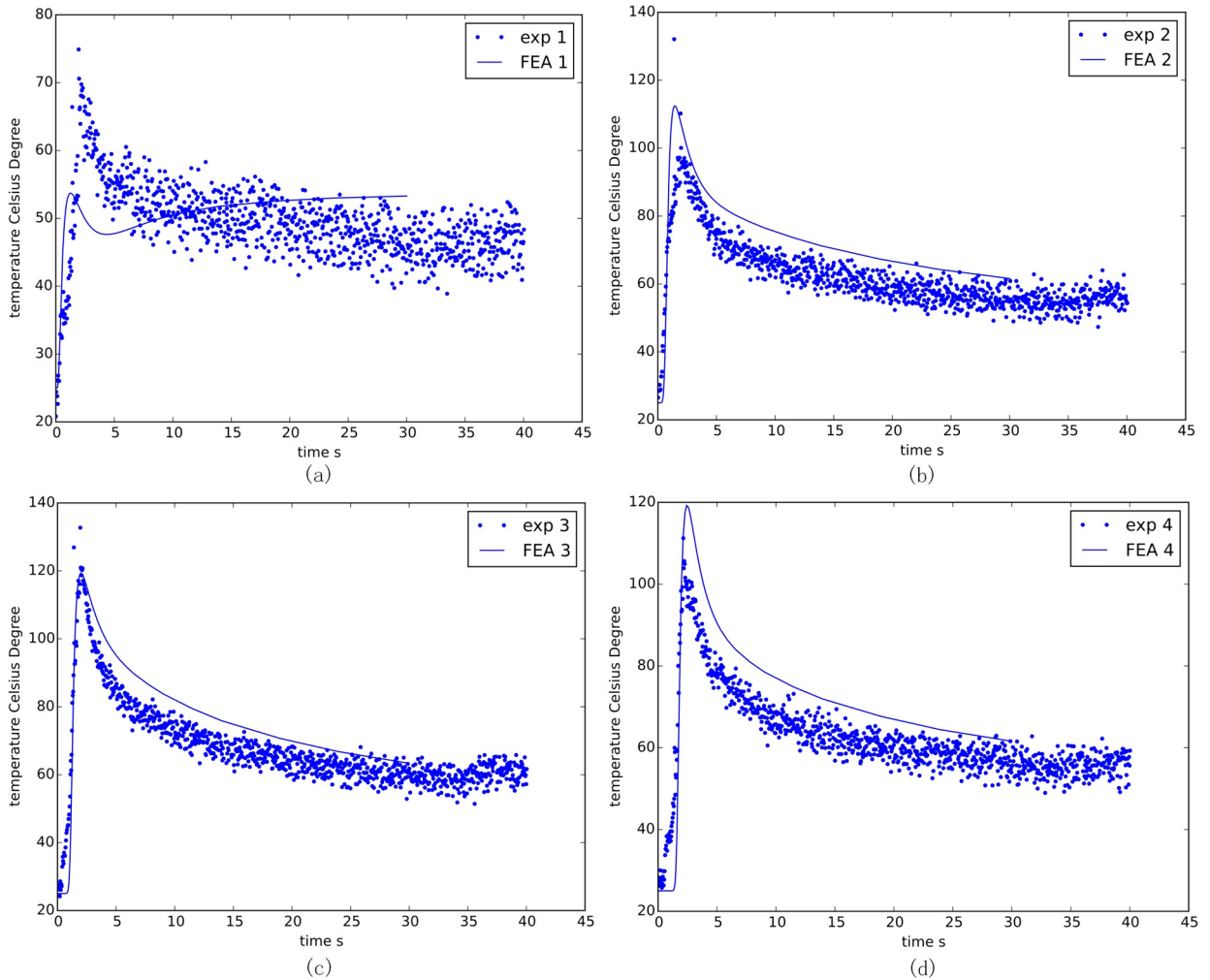

Fig. 9. Temperature validation with four type-K thermocouples. (a), (b), (c) and (d) are measured at locations 1, 2, 3, and 4, respectively.

"decentered polygon" algorithm does not need to create square for each cell when it begins to grow. Only the decentered polygon of a starting nucleated cell is tracked during the grain growth process, which reduces the computation cost. Besides, the modified algorithm can prevent grain orientations from realigning with the x axis after a few growing steps because each cell will stop growing when its Von Neumann and Moore neighbors are both solid. The controlling point growth rate is determined by the local cell temperature. Therefore, the region with higher thermal gradient will solidify faster along the steepest thermal gradient.
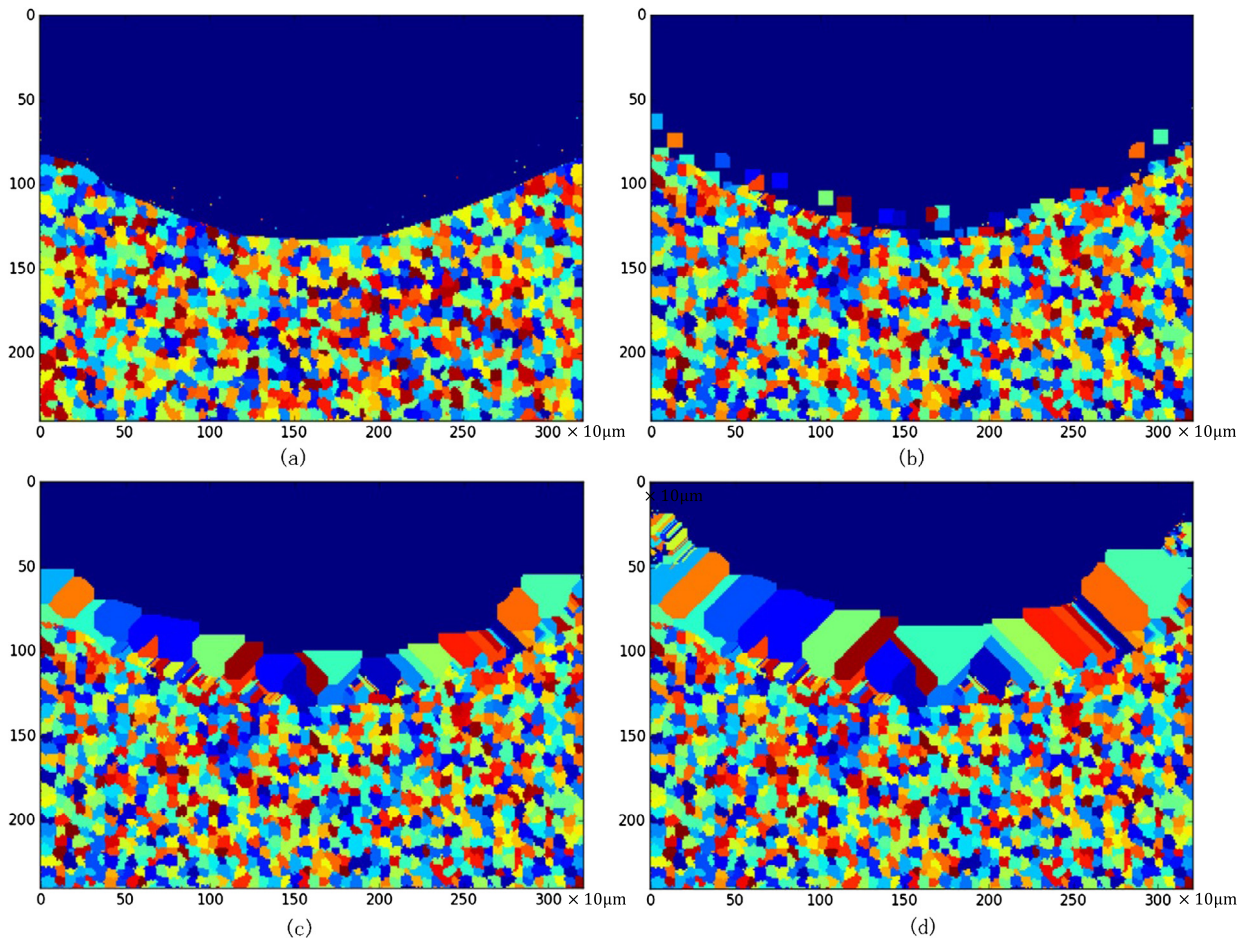
Fig. 10. Grain structure obtained using the conventional growth method for single-layer Ti6Al4V deposition at (a) 5-ms (b) 25-ms (c) 45-ms, and (d) 65-ms time steps.

3. Results and discussion

3.1. Single-layer temperature and grain structure

The deposition temperature field and grain morphology were simulated first only in one layer. Fig. 6 shows the thermal history of the whole block during the DMD process. Fig. 6a indicates the temperature field of the whole block when the laser beam is passing along the *x* direction at time = 1.0 s, while Fig. 6b shows the temperature field when the substrate cools down with laser off at time = 29.0 s. The total physical time of one-layer laser deposition is 2 s, while the cooling time is 28 s in the simulation. For each step, the step time is 0.1 s when the laser is shot on the surface of the deposited material. After 30 s of cooling down, the temperature distribution is more uniform. Fig. 7 indicates the thermal history of two nodes, which locate at the center point in the deposit and 1 mm away from the deposit. The result shows that the highest temperature in the deposit is approximately 2884 K, which occurred at the center of the Gaussian beam. The center node at 1 mm away from the deposit arrives at a peak temperature of 1126 K that cannot melt the Ti6Al4V substrate. Based on every node's thermal history, the undercooling (discrepancy between liquidus temperature and current temperature) that is critical to grain nucleation and growth rate can be determined.

So that the input of microstructure model is reliable, the temperature field is validated with four type-K thermocouples. The locations are shown in Fig. 8. One is located at the starting end of the laser path. Another three points are located by one side of the laser path. Arduino's device is used to sample the temperature data. The TC position is near to the melt pool. The distance is 3~3.5 mm. A laser deposition experiment is conducted with a power of 750 W, a scanning speed of 600 mm/min and 2 g/min for single-layer deposit. The difference between experiment and FEM modeling is less than 10 Celsius degrees, as shown in Fig. 9. In the real experiment, the substrate is fixed by the metal fixture, which results in greater heat conduction than in the FEM model. Because of argon gas, forced convection occurred in the real experiment. This also causes a lower cooling rate in the temperature simulation. Because the difference between experiment and simulation is
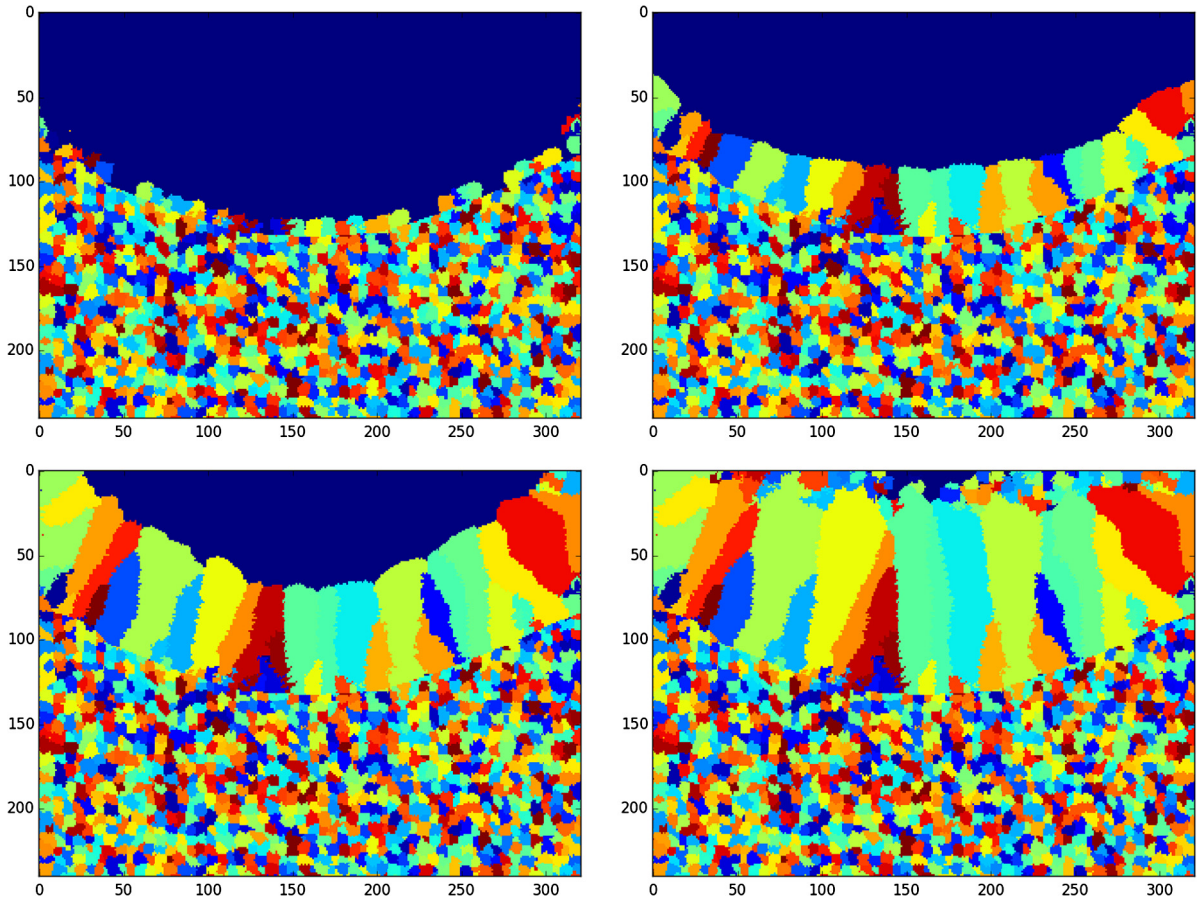
Fig. 11. Grain structure obtained using the developed growth method for single-layer Ti6Al4V deposition at (a) 20-ms (b), 40-ms, (c) 60-ms, and (d) 80-ms time steps.
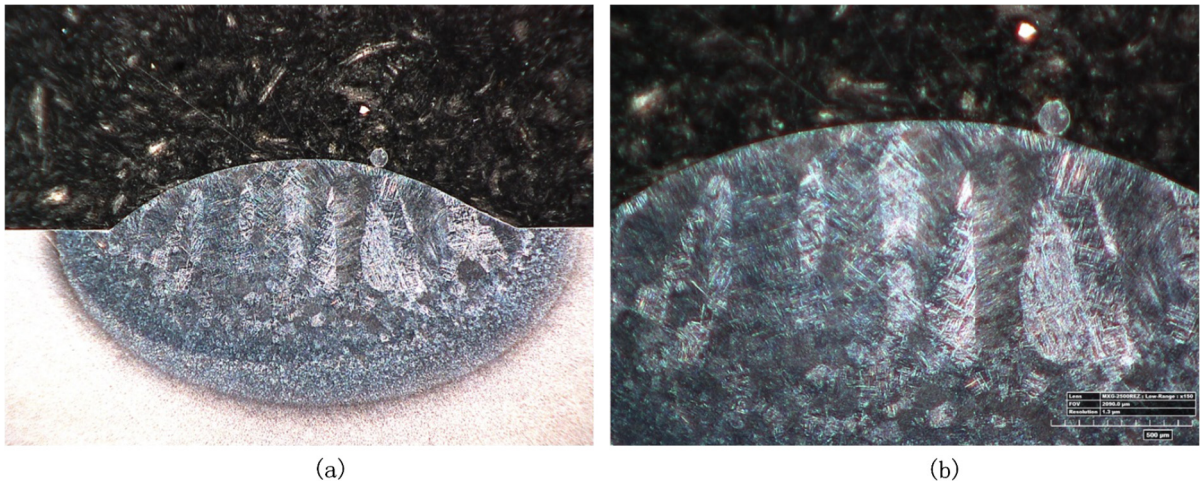

Fig. 12. Ti–6Al–4V grain morphology obtained by single-layer deposition: (a) 50 ×; (b) 200 ×.

smaller than 10%, the current FEA modeling is still considered as a reasonable simulation of the temperature field, which can provide the reliable thermal input for the CA model.

A laser deposition experiment is conducted with a power of 700 W, a scanning speed of 600 mm/min and 2 g/min for a single-layer deposit. For this case, the cross section shown in the figure is the computational domain. The cell size for this simulation is 6 μm × 6 μm. The X and Y axes represent the number of cells. The simulation result obtained using
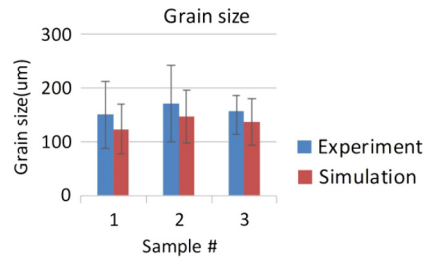
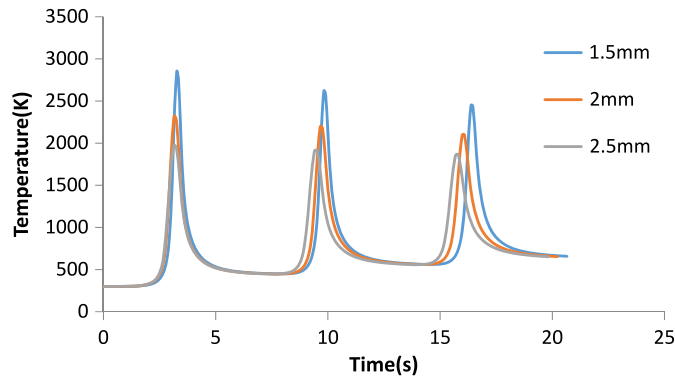**Fig. 13.** Grain size comparison between simulation and experiment.

Fig. 14. Laser diameter sensitivity analysis.

the conventional method is shown in Fig. 10. It can be observed that, even though different grains take diverse orientations at the very beginning, the crystallographic orientation preference tends to be along the axis after several time steps. Here, different colors represent various grain orientations. Finally, the equiaxed grains dominate the fusion zone. The original grain orientations are not kept during the solidification process. It does not agree well with the single-layer experimental result shown in Fig. 12.

The developed CA grain growth method is implemented under the same conditions. According to the developed CAFÉ simulation, the single layer simulation result is shown in Fig. 11. The grain keeps its original crystallization orientation when the grain growth is modeled. The columnar grain can be identified from the solid/liquid interface. When grains continue to grow towards the melt pool center, some grains overgrow other grains in such a way that there are fewer grains further away from the solid/liquid interface.

Three samples of single-layer deposits are prepared with EDM cutting, grinding, polishing, and etching. The optical microscope is shown in Fig. 12. The comparison between simulation and experimental results is shown in Fig. 13. An average of twenty measurements per sample is performed to determine the average grain size number. It compares the experimental average grain size number with the predicted average grain size number. The shown data suggests that a 15% error between measurements and predictions is present. This can be considered as a reasonable prediction of grain morphology and size.

3.2. Sensitivity analysis

In the thermal model, the Gaussian distribution heat source is simulated. The laser diameter is determined by the location of $1/e^2$ of maximum intensity. Three cases from 1.5 mm to 2.5 mm are shown in Fig. 14. It can be seen that the bottom temperatures are the same because the input total energies are the same. The diameter difference directly influences the energy density of the heat source. Therefore, the peak temperature for three cases are different. At 2.5 mm, the temperature peak is delayed least since a larger diameter makes that the measured center point is affected earlier, in such a way that it arrives at the peak value earliest. For Fig. 15, the influence of temperature is analyzed. The combined equation is $h \approx 2.41 \times 10^{-3} \varepsilon T^{1.61}$, whose power is 1.61. Power changes from 1.2 to 3. It can be observed that the valley temperature varies among different power cases. Power directly affects the combined heat transfer coefficient. When the model employs a higher of power value, heat is dissipated faster. Therefore, the valley temperature will be lower. However, for the peak temperature difference, it is approximately 300 K, which is not as obvious as in Fig. 14. For peak temperature, heat source distribution plays a much more important role.

In the CA model, the initial grain size effect on the final grain morphology in the fusion zone is analyzed in Fig. 16. The three grain sizes are 20 μm, 40 μm, and 80 μm. It can be seen that, as the initial grain size de-
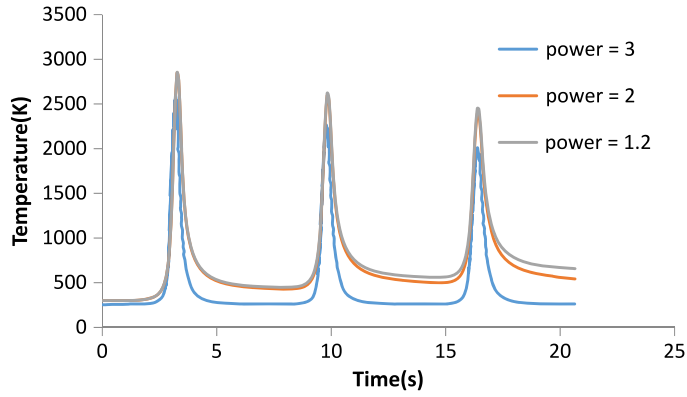
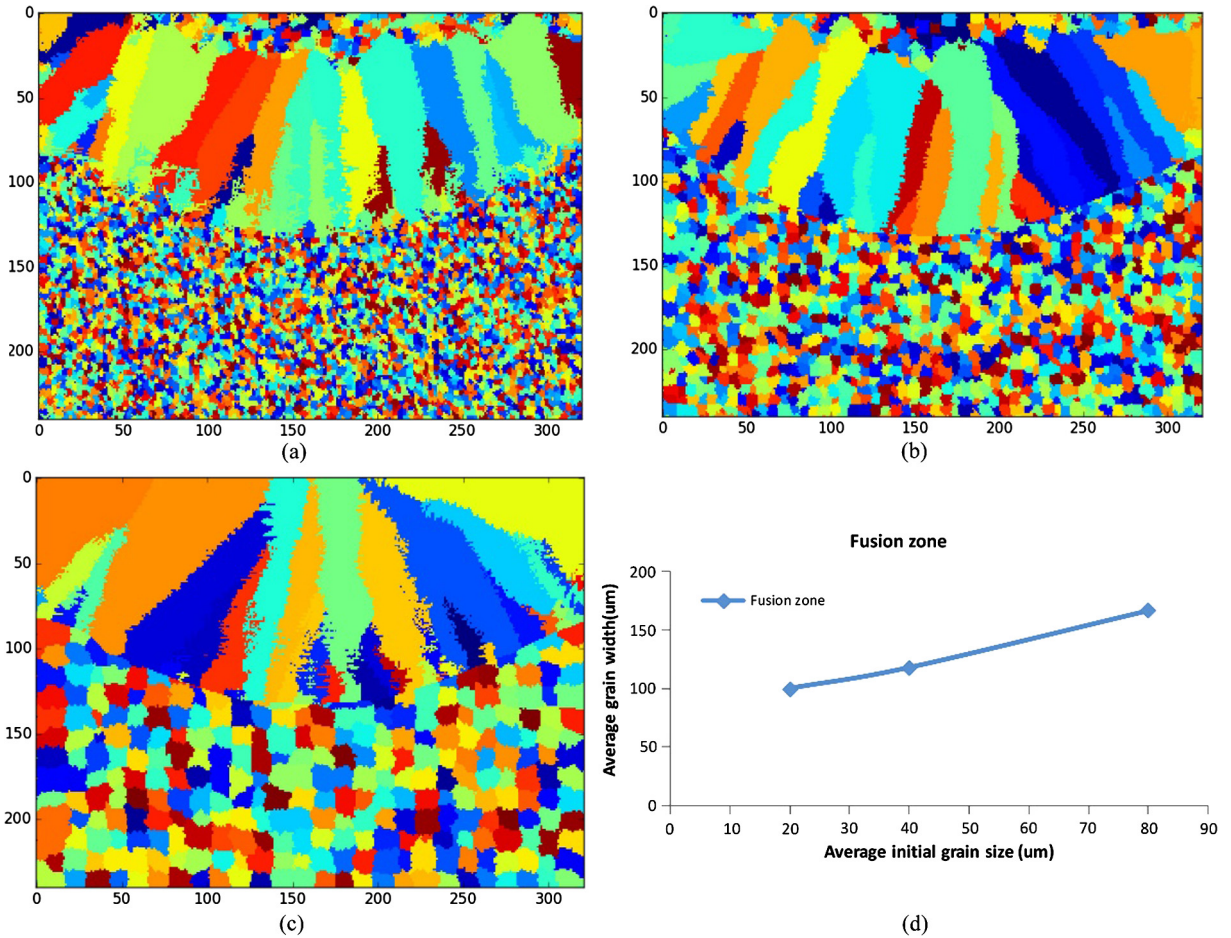**Fig. 15.** Temperature power sensitivity analysis.

Fig. 16. Initial grain size vs. fusion zone grain width. (a) 20 µm, (b) 40 µm, (c) 80 µm, (d) relationship between initial grain size with final grain width.

creases, the average grain width also decreases. In contrast to homogeneous nucleation, where every atom in the liquid is a potential nucleation site, the number of sites for heterogeneous nucleation depends on the amount and type of the foreign substrate. A large initial grain size limits available nucleation sites for FZ grains. There is less nucleation occurrence at the liquid/solid interface. Competition between the grains ensures that further growth follows similar trends. Compared to the electron beam welding process in the reference, the similar trend is identified [5].

The quantitative simulation of CET relies upon the density and activity of the heterogeneous nuclei. To illustrate the importance of the nucleation parameters (and hence grain refining), the effect of reducing the barrier to nucleation (i.e.
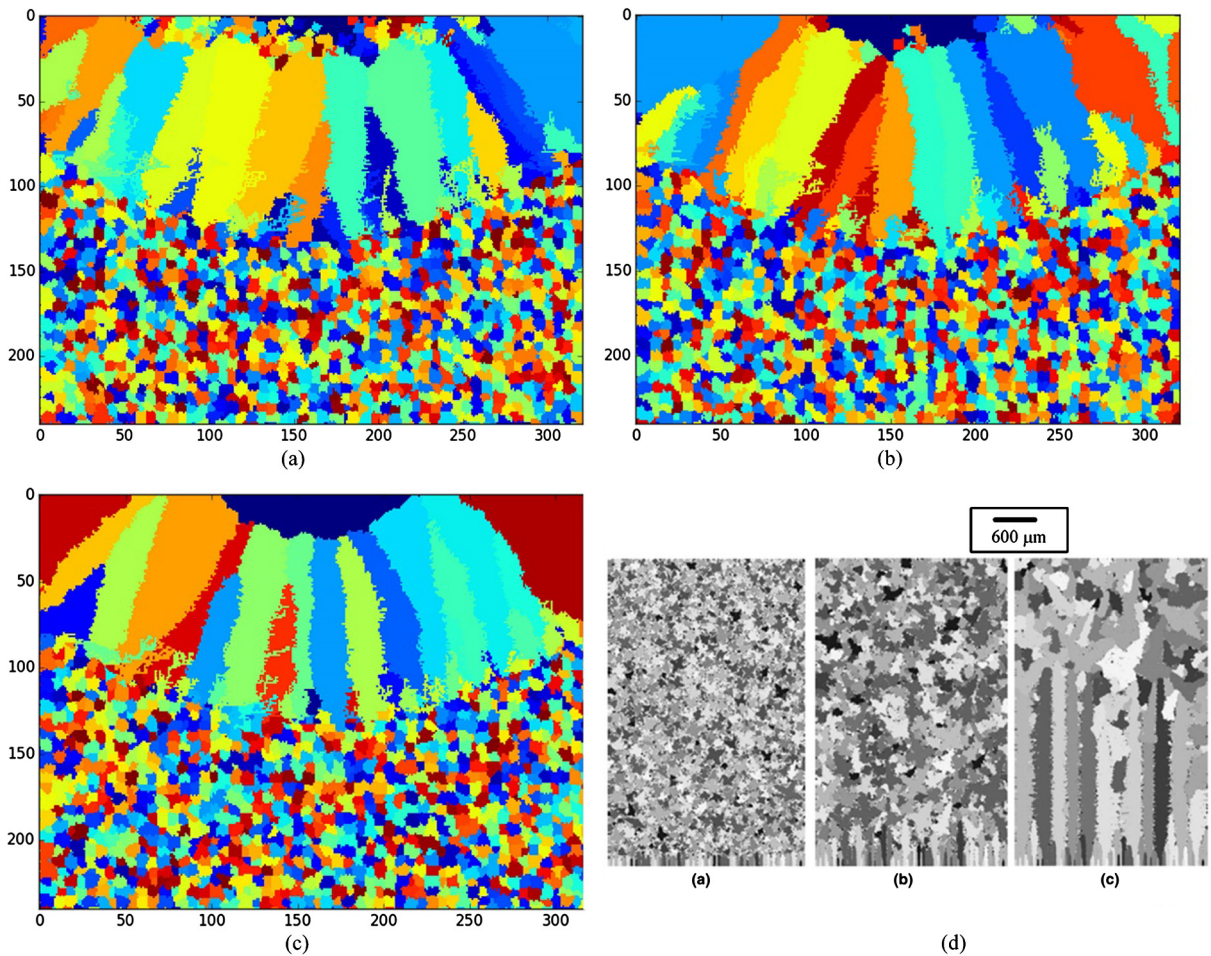
Fig. 17. Mean nucleation undercooling effect on grain structure.

ΔT_N) from the base cases of ΔT_N equal to 5 K to 10 K and 20 K is shown in Fig. 17. A decrease in the mean nucleation undercooling favors the formation of equiaxed grains at the top. When the mean undercooling is low, there are more opportunities for nucleation in the top liquid bulk before columnar grains dominate this region.

For the columnar grains' growth, the grain misorientation information is also analyzed. This is the six-layer deposit simulation from the front view. Fig. 18 shows the evolution of the grain texture as a function of the built height. It is clearly seen that starting from an equiaxed baseplate with no texture at low height, a strong texture develops due to grain selection with increasing built height. Within the red dashed rectangle region, the high misorientation becomes less in the top deposit area. But in the region close to the substrate, low and high misorientations both exist because grain overgrowth has not occurred in this region.

4. Conclusions

The transient temperature field of one-layer and multiple-layer deposition of Ti–6Al–4V was simulated with a finite element method. The simulation result was validated by a thermocouple experiment. The FE model provides the temperature at a relatively coarse scale (200 μm) and an interpolation algorithm was used to scale the temperature field to match that of the CA model. The FE–CA model predicts grain morphology evolution as the deposition cools down. Hence, the instantaneous nucleation law, grain growth, and crystallographic orientation were modeled in this study. It has been found that the developed "decentered polygon" growth method is more appropriate for the highly non-uniform temperature field, and the simulation result is closer to the real experimental measurement compared to conventional growth methods. The grain sizes of the single layer are similar in simulation and in experiment. This demonstrates that this FE–CA simulation can reasonably predict the thermal history and grain morphology during this case of direct metal deposition.
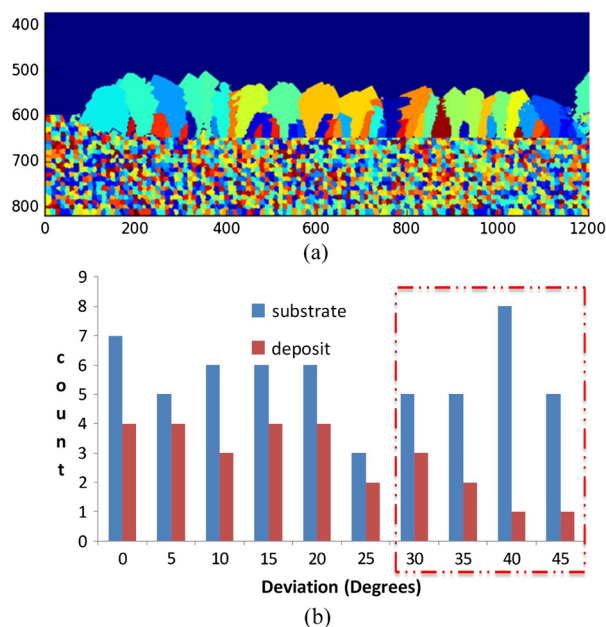
Fig. 18. Deviation degrees of grains from substrate to deposit.

References

[1] M. Rappaz, Modelling of microstructure formation in solidification processes, Int. Mater. Rev. 34 (3) (1989) 93–124.
[2] M.P. Anderson, D.J. Srolovitz, G.S. Grest, P.S. Sahni, Computer simulation of grain growth, I: kinetics, Acta Metall. 32 (5) (May 1984) 783–791.
[3] D.J. Srolovitz, M.P. Anderson, P.S. Sahni, G.S. Grest, Computer simulation of grain growth, II: grain size distribution, topology, and local dynamics, Acta Metall. 32 (5) (1984) 793–802.
[4] Y. Saito, M. Enomoto, Monte Carlo simulation of grain growth, ISIJ Int. 32 (3) (1992) 267–274.
[5] L.-Q. Chen, Phase-Field Models for Microstructure Evolution, 2002.
[6] C.E. Krill III, L.-Q. Chen, Computer simulation of 3-D grain growth using a phase-field model, Acta Mater. 50 (12) (2002) 3059–3075.
[7] B. Böttger, J. Eiken, I. Steinbach, Phase field simulation of equiaxed solidification in technical alloys, Acta Mater. 54 (10) (2006) 2697–2704.
[8] N. Moelans, B. Blanpain, P. Wollants, An introduction to phase-field modeling of microstructure evolution, Calphad 32 (2) (Jun. 2008) 268–294.
[9] S. Sahoo, K. Chou, Phase-field simulation of microstructure evolution of Ti–6Al–4V in electron beam additive manufacturing process, Addit. Manuf. 9 (2016) 14–24.
[10] J. Nandy, H. Sarangi, S. Sahoo, Microstructure evolution of Al–Si–10Mg in direct metal laser sintering using phase-field modeling, Adv. Manuf. 6 (1) (2018) 107–117.
[11] M. Rappaz, C.-A. Gandin, Probabilistic modelling of microstructure formation in solidification processes, Acta Metall. Mater. 41 (2) (1993) 345–360.
[12] C.-A. Gandin, M. Rappaz, A coupled finite element-cellular automaton model for the prediction of dendritic grain structures in solidification processes, Acta Metall. Mater. 42 (7) (1994) 2233–2246.
[13] C.-A. Gandin, J.-L. Desbiolles, M. Rappaz, P. Thevoz, A three-dimensional cellular automation-finite element model for the prediction of solidification grain structures, Metall. Mater. Trans. A 30 (12) (1999) 3153–3165.
[14] A. Choudhury, K. Reuther, E. Wesner, A. August, B. Nestler, M. Rettenmayr, Comparison of phase-field and cellular automaton models for dendritic solidification in Al–Cu alloy, Comput. Mater. Sci. 55 (2012) 263–268.
[15] X. Doré, Modelling of microsegregation in ternary alloys: application to the solidification of Al–Mg–Si, Acta Mater. 48 (15) (2000) 3951–3962.
[16] D.J. Jarvis, S.G.R. Brown, J.A. Spittle, Modelling of non-equilibrium solidification in ternary alloys: comparison of 1D, 2D, and 3D cellular automaton-finite difference simulations, Mater. Sci. Technol. 16 (11–12) (2000) 1420–1424, 2000.
[17] M. Grujicic, G. Cao, R.S. Figliola, Computer simulations of the evolution of solidification microstructure in the LENS^{TM} rapid fabrication process, Appl. Surf. Sci. 183 (2001) 43–57.
[18] S.M. Kelly, S.L. Kampe, Microstructural evolution in laser-deposited multilayer Ti–6Al–4V builds, part I: microstructural characterization, Metall. Mater. Trans. A 35 (6) (2004) 1869–1879.
[19] S.M. Kelly, S.L. Kampe, Microstructural evolution in laser-deposited multilayer Ti–6Al–4V builds, part II: thermal modeling, Metall. Mater. Trans. A 35 (6) (2004) 1869–1879.
[20] W. Tan, Y.C. Shin, Multi-scale modeling of solidification and microstructure development in laser keyhole welding process for austenitic stainless steel, Comput. Mater. Sci. 98 (Feb. 2015) 446–458.
[21] S. Chen, G. Guillemot, C.-A. Gandin, 3D coupled cellular automaton (CA)-finite element (FE) modeling for solidification grain structures in gas tungsten arc welding (GTAW), ISIJ Int. 54 (2) (2014) 401–407.
[22] S. Chen, G. Guillemot, C.-A. Gandin, Three-dimensional cellular automaton-finite element modeling of solidification grain structures for arc-welding processes, Acta Mater. 115 (2016) 448–467.
[23] A. Zinoviev, O. Zinovieva, V. Ploshikhin, V. Romanova, R. Balokhonov, Evolution of grain structure during laser additive manufacturing. Simulation by a cellular automata method, Mater. Des. 106 (2016) 321–329.
[24] G. Lütjering, Influence of processing on microstructure and mechanical properties of $(\alpha + \beta)$ titanium alloys, Mater. Sci. Eng. A 243 (1–2) (1998) 32–45.
[25] J.N. Reddy, D.K. Gartling, The Finite Element Method in Heat Transfer and Fluid Dynamics, 3rd edition, CRC Press, Taylor & Francis Group, Boca Raton, FL, USA, 2010.
[26] L.C.A.R.L. Phillips, Laser Beam Propagation Through Random Media, vol. PM152, 2nd edition, SPIE Press Book Monograph, 2005.

[27] M. Alimardani, E. Toyserkani, J.P. Huissoon, A 3{D} dynamic numerical approach for temperature and thermal stress distributions in multilayer laser solid freeform fabrication process, Opt. Lasers Eng. 45 (12) (2007) 1115–1130.

[28] C. Lampa, A.F.H. Kaplan, J. Powell, C. Magnusson, An analytical thermodynamic model of laser welding, J. Phys. D, Appl. Phys. 30 (9) (1997) 1293.

[29] H. Liu, T. Sparks, Modeling and verification of temperature distribution and residual stress in laser aided metal deposition process, 4th Intelligent Systems Center 1 (2012) 1–7.

[30] W. Oldfield, A quantitative approach to casting solidification: freezing of cast iron, Trans. Amer. Soc. Met. 59 (1966) 945.

[31] W. Kurz, D.J. Fisher, Appendix 7 and 8, in: Fundamentals of Solidification, Trans. Tech. Publication, 1992, pp. 226–246.

[32] W. Kurz, D.J. Fisher, Appendix 9, in: Fundamentals of Solidification, Trans. Tech. Publication, 1992, pp. 247–260.

[33] R. Chen, Q. Xu, B. Liu, A modified cellular automaton model for the quantitative prediction of equiaxed and columnar dendritic growth, J. Mater. Sci. Technol. 30 (12) (2014) 1311–1320.